3-28-2016

Direct Collapse to Supermassive Black Hole Seeds: Comparing the AMR and SPH Approaches

Yang Luo
Osaka University, Japan

Kentaro Nagamine
Osaka University, Japan

Isaac Shlosman
University of Kentucky, shlosman@pa.uky.edu

Monthly Notices
of the
ROYAL ASTRONOMICAL SOCIETY

MNRAS **459,** 3217–3233 (2016)
Advance Access publication 2016 March 28

doi:10.1093/mnras/stw698

Direct collapse to supermassive black hole seeds: comparing the AMR and SPH approaches

Yang Luo,[1]★ Kentaro Nagamine[1,2] and Isaac Shlosman[1,3]★

[1]*Theoretical Astrophysics, Department of Earth & Space Science, Osaka University, 1-1 Machikaneyama, Toyonaka, Osaka 560-0043, Japan*
[2]*Department of Physics & Astronomy, University of Nevada Las Vegas, 4505 S. Maryland Pkwy, Las Vegas, NV 89154-4002, USA*
[3]*Department of Physics & Astronomy, University of Kentucky, Lexington, KY 40506-0055, USA*

Accepted 2016 March 22. Received 2016 March 22; in original form 2015 December 10

ABSTRACT

We provide detailed comparison between the adaptive mesh refinement (AMR) code ENZO-2.4 and the smoothed particle hydrodynamics (SPH)/*N*-body code GADGET-3 in the context of isolated or cosmological direct baryonic collapse within dark matter (DM) haloes to form supermassive black holes. Gas flow is examined by following evolution of basic parameters of accretion flows. Both codes show an overall agreement in the general features of the collapse; however, many subtle differences exist. For isolated models, the codes increase their spatial and mass resolutions at different pace, which leads to substantially earlier collapse in SPH than in AMR cases due to higher gravitational resolution in GADGET-3. In cosmological runs, the AMR develops a slightly higher baryonic resolution than SPH during halo growth via cold accretion permeated by mergers. Still, both codes agree in the build-up of DM and baryonic structures. However, with the onset of collapse, this difference in mass and spatial resolution is amplified, so evolution of SPH models begins to lag behind. Such a delay can have effect on formation/destruction rate of H_2 due to UV background, and on basic properties of host haloes. Finally, isolated non-cosmological models in spinning haloes, with spin parameter $\lambda \sim 0.01$–0.07, show delayed collapse for greater λ, but pace of this increase is faster for AMR. Within our simulation set-up, GADGET-3 requires significantly larger computational resources than ENZO-2.4 during collapse, and needs similar resources, during the pre-collapse, cosmological structure formation phase. Yet it benefits from substantially higher gravitational force and hydrodynamic resolutions, except at the end of collapse.

Key words: methods: numerical – galaxies: formation – galaxies: high-redshift – cosmology: theory – dark ages, reionization, first stars.

1 INTRODUCTION

The origin of supermassive black holes (SMBHs) in the galactic centres remains an unresolved problem in astrophysics. Unless the SMBHs are primordial, a number of alternative scenarios exist. First, they could grow from relics of the Population III stars (e.g. Madau & Rees 2001; Abel, Bryan & Norman 2002; Bromm & Larson 2004; Volonteri & Rees 2005) – the largely pre-galactic objects whose masses appear to be comparable or slightly higher than normal OB stars (e.g. Turk, Abel & O'Shea 2009; Hosokawa et al. 2011; Wise et al. 2012; Hirano et al. 2014; Fraser et al. 2015, see also Bromm 2013 for review). Secondly, they could form from the runaway collapse of compact stellar clusters, subject to general relativistic effects (e.g. Zel'dovich & Podurets 1965; Shapiro & Teukolsky 1985), or stellar/gasdynamics evolution of stellar clusters (e.g. Begelman & Rees 1978). Most appealing, however, is the third alternative which involves a direct baryonic collapse to form massive black hole seeds of $\sim 10^4$–10^7 $M_\odot$ (e.g. Haehnelt & Rees 1993; Loeb & Rasio 1994; Bromm & Loeb 2003; Koushiappas, Bullock & Dekel 2004; Begelman, Volonteri & Rees 2006; Volonteri & Rees 2006; Begelman, Rossi & Armitage 2008; Begelman & Shlosman 2009; Milosavljević et al. 2009; Mayer et al. 2010; Schleicher, Spaans & Glover 2010; Johnson et al. 2011; Choi, Shlosman & Begelman 2013, 2015; Latif et al. 2013; Prieto, Jimenez & Haiman 2013; Shlosman et al. 2016), which experience a substantial growth subsequently. Depending on the chemical composition of the collapsing gas, this can take place when suitable dark matter (DM) haloes appear in the universe. For a primordial composition, hydrogen can be either atomic, with a cooling floor of just below 10^4 K, or molecular, which is able to cool down by additional $\sim$2 orders of magnitude. In the former case, for the gas to collapse, the virial

★E-mail: yluo@vega.ess.sci.osaka-u.ac.jp (YL); shlosman@pa.uky.edu (IS)

temperature of DM haloes must exceed the cooling floor of hydrogen, with the corresponding mass of $\sim 10^8$ $M_\odot$. In the latter case, the critical halo masses will be smaller.

Direct collapse scenario involves gravitational collapse from typical spatial scales of ∼1 kpc, down to ∼1–100 Schwarzschild radii of the seed SMBH – an enormous dynamic range. Solution of the full problem requires application of the coupled radiative hydrodynamics of the collapsing matter, magneto-hydrodynamics (MHD), and other ingredients, and cannot be accomplished analytically. Here we limit ourselves to the hydrodynamical and radiation part of the problem, and, in addition, assume that the collapsing gas is optically thin to its own produced radiation. The heavily computational approach employed by various groups to address this and related issues involves different numerical algorithms. These include the adaptive mesh refinement (AMR) and smoothed particle hydrodynamics (SPH) codes, which are semi-Eulerian and Lagrangian, respectively. In this work, we compare the efficiency and reliability of two representative codes, ENZO-2.4 AMR code (Bryan & Norman 1997; Norman & Bryan 1999; Bryan et al. 2014), and modified version of GADGET-3 SPH/*N*-body code (Springel 2005).

Previous comparison between the grid and Lagrangian codes have both achieved results within ∼20 per cent, in the cosmological context (e.g. O'Shea et al. 2005), and also found significant differences. One of the primary results that they found was that the AMR requires significantly greater computational resources in order to achieve the same DM halo mass function as in the SPH code. This was due to the lower force resolution in the AMR code at early times than in SPH code, which resulted in the lack of early growth of density perturbations at high redshifts.

In the Santa Barbara Cluster Comparison project (Frenk et al. 1999), different groups have simulated formation of one galaxy cluster from identical initial conditions (ICs). In this case, for example, the central entropy profile (within the virial radius) presents a floor in grid codes, whereas such feature is absent in the SPH codes. These discrepancies remain largely unexplained although more recent works have improved significantly the agreement by using the entropy-conserving version of SPH codes (e.g. Ascasibar et al. 2003; Springel & Hernquist 2003; Vogelsberger et al. 2012). The ongoing AGORA project of a broad comparison between a number of grid and Lagrangian codes of well-resolved galaxies focuses on convergence study of various feedback processes (Kim et al. 2014). However this comparison project is in its early stage.

Statistics of driven supersonic turbulence at a high Mach number have been performed by Price & Federrath (2010) using FLASH, a widely used Eulerian grid-based AMR code, and the SPH code PHANTOM. Excellent agreement between these codes has been found at similar number of particles and grid cells for the basic statistical properties of the turbulence, such as the slope in the velocity power spectrum, lognormal probability distribution function (PDF), the width of the PDF, etc. At the same time, SPH code has shown a better spatial resolution. Dense structures have been resolved already with 128^3 SPH particles, compared to 512^3 cells required for the same purpose in AMR. Unfortunately, this comparison differs fundamentally from the one performed in this work: it is entirely non-gravitational. As a result, the density stratification was much weaker than what one observes during gravitational collapse, and hence the evolution in their simulation did not go as far as in our current work.

It remains unclear, whether SPH or AMR codes are more accurate in general simulation regimes. Both methods have their shortcomings. For example, in AMR, if the fluid moves rapidly across the mesh, the truncation errors lead to significant departure from the same simulation if there is no bulk velocity (Tasker et al. 2008). Hopkins (2013) have studied a number of SPH modifications, in particular alternative SPH equations of motion that guarantee conservation and improved treatment of fluid contact discontinuities (e.g. Kelvin–Helmholtz instability). Good agreement has been reported for supersonic flows and associated strong shocks, but the SPH suppresses mixing in subsonic thermal pressure-dominated regimes. Saitoh & Makino (2013) have also provided a new density-independent formulation of SPH which removes the artificial surface tension. Their method was more formally treated in the Lagrangian formalism by Hopkins (2013).

Another important issue for classical AMR codes is the angular momentum conservation. Unless we can anticipate the geometry of the flow and adjust accordingly the mesh so that the fluid velocity is perpendicular to the boundary, the accuracy is seriously compromised and subject to artificially enhanced diffusion. Finally, the refinement criteria is somewhat arbitrary and can produce various artefacts. At the refinement boundaries, there is a significant loss of accuracy as the refinement is necessarily discontinuous.

On the other hand, the SPH in 3D suffers from a poor shock resolution, noise on the scale of the smoothing kernel, and low-order accuracy for the treatment of contact discontinuities. Hydrodynamic instabilities like the Kelvin–Helmholtz can be suppressed (Agertz et al. 2007), although recent modifications put forth by Hopkins (2013) have been claimed to correct these problems. In real fluids, the entropy is raised in shocks because particle collisions randomize their velocities which increase the heat and the entropy. The SPH does not capture shocks properly because entropy must be generated locally to dissipate the small-scale velocities. In order to mimic this process, and to prevent interpenetration of the SPH particles at the shock locations, artificial viscosity is required. The introduction of the latter usually results in an overly viscous fluid away from shocked regions. To overcome this, the Balsara (1995) switch or Cullen & Dehnen (2010) formulation have been developed.

The aim of this paper is to compare the ability of AMR and SPH codes in following the direct collapse of gas with a primordial composition, i.e. involving identical atomic hydrogen cooling. We compute and analyse models of gas collapse inside DM haloes in isolated and cosmological settings. Our models span more than seven orders of magnitude in radius, from 1 kpc down to 10^{-4} pc. Of course, the main question is whether both codes can describe the evolution that leads to the same end product. However, specific details are important as well, namely are various physical quantities (e.g. gas density, temperature, tangential and radial velocity, and angular momentum distributions) similar at various times of the collapse? Does it take the same time to collapse, and how do accretion rates and their temporal and radial distributions compare?

This paper is structured as follows. In Section 2, we briefly describe the AMR and SPH codes used. Section 3 provides the results of our comparison runs, and in the last section, we discuss our results and summarize them.

2 NUMERICAL TECHNIQUES

2.1 ENZO AMR and GADGET-3 SPH

The AMR code ENZO-2.4 has been tested extensively and is publicly available. It uses a multigrid particle-mesh *N*-body method to calculate the gravitational dynamics, including collisionless DM particles, and a second-order piecewise parabolic method (PPM; Colella & Woodward 1984; Bryan et al. 1995) to solve hydrodynamics. ZEUS hydro is also available, but we use PPM here.

The structured AMR used in ENZO places no fundamental restrictions on the number of rectangular grids used to cover some region of space at a given level of refinement, or on the number of refinement levels (Berger & Colella 1989). A grid is refined by a factor of 2 in lengthscale, if either the gas or DM density become greater than $\rho_0 N^\ell$, where ρ_0 is the cosmic mean density for the gas or DM, respectively. The refinement factor is $N = 2$, and ℓ refers to the AMR refinement level.

The Jeans length has been resolved by at least four cells in these simulations to satisfy the Truelove et al. (1997) requirement for resolution. For the SPH code, an equivalent criterion is to resolve the local Jeans mass by having at least twice the number of particles in an SPH kernel (Bate & Burkert 1997).

In GADGET-3, the gas and the DM are represented by particles. The *N*-body solver is essentially the same as in GADGET-2 (Springel 2005), with some improvements for optimization purposes, such as the domain decomposition. To achieve the spatial adaptivity at a moderate computational cost, it uses a hierarchical multipole expansion, i.e. the tree algorithm (Barnes & Hut 1986). The gravitational potential is softened below a spatial scale specified by the gravitational softening length. In principle, this kernel (and the associated softening length, ϵ, which represents the force resolution) can differ from the smoothing length used in the hydrodynamical method, as we describe below. But mostly the SPH uses the same cubic-spline kernel, with a fixed ϵ evaluated as the mean initial interparticle distance, divided by a fudge factor of ∼20–30.

We use GADGET-3 with the density-independent SPH version with a quintic kernel and time-independent viscosity (Hopkins 2013). Comparison of various viscosity algorithms has been performed by Cullen & Dehnen (2010), who proposed a new artificial viscosity prescription. This viscosity grows rapidly in strong shocks, and decays rapidly away from the shocks to a minimum $\alpha = 0.2$, compared to usual constant artificial viscosity. With this method, the gas becomes virtually inviscid away from the shocks, while maintaining particle order. The viscosity decay length is taken as 3.73, and the source scaling equal to 2.77.

For the cooling package, we use GRACKLE version 2.0 for GADGET-3, and GRACKLE version 1.1 for ENZO. These versions for the SPH and AMR codes have identical chemistry and cooling (Bryan et al. 2014; Kim et al. 2014, https://grackle.readthedocs.org/). This library was born out of the chemistry and cooling routines of the ENZO simulation code. The GRACKLE solves for radiative cooling and internal energy, calculates cooling time, temperature, pressure, and ratio of specific heats. It uses a non-equilibrium primordial chemistry network for atomic H and He (Abel et al. 1997; Anninos et al. 1997), H_2 and HD, Compton cooling off the cosmic microwave background, tabulated metal cooling and photoheating rates calculated with CLOUDY (Ferland et al. 2013). In addition, GRACKLE provides a look-up table for equilibrium cooling. The gas is assumed to be dust free and optically thin and the metals are assumed to be in ionization equilibrium. The cooling rate for a parcel of gas with a given density, temperature, and metallicity, that is photoionized by incident radiation of known spectral shape and intensity can be precalculated. As we focus on gravitational collapse models at $z > 10$, and limit the runs to the optically-thin regime, the UV background is not included, and we neglect the radiative transfer of ionizing photons in this work.

2.2 Set-up in isolated models

For isolated models, we adopt the *WMAP*5 cosmological parameters (Komatsu et al. 2009), namely, $\Omega_m = 0.279$, $\Omega_b = 0.0445$, $h = 0.701$,

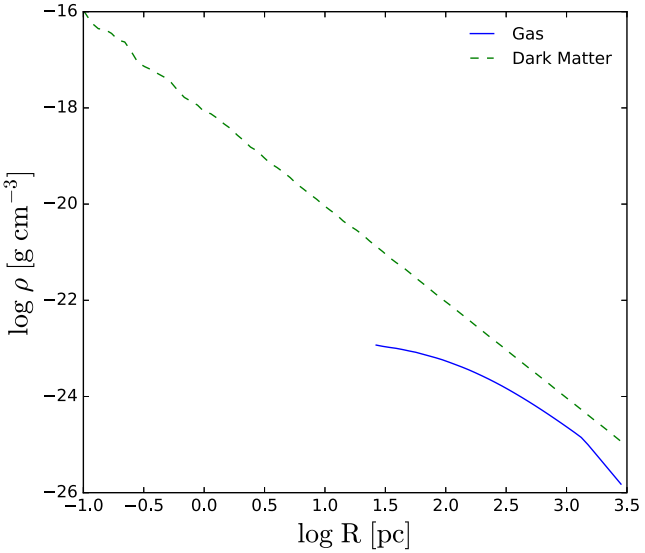

Figure 1. Initial density profiles in the isolated halo model for the gas (solid line) and DM (dashed line) as a function of radius.

where h is the Hubble constant in units of $100\,\mathrm{km\,s^{-1}\,Mpc^{-1}}$. We set up the details of an isolated DM halo that is consistent with the cosmological context that we work with. Therefore, some of the halo parameters are specified with units that include the Hubble parameter, although we use physical quantities (not comoving) in all isolated case calculations. In both codes, we define a DM halo as having the density equal to the critical density Δ_c times the mean density of the universe, ρ_b, which depends on the redshift z and the cosmological model. The top-hat model is used to calculate $\Delta_c(z)$, and the density is calculated within a virial radius, R_{vir}. The halo virial mass is $M_{vir}(z) = (4\pi/3)\Delta_c(z)\rho_b R_{vir}$.

For isolated models we work in physical coordinates. We assume that the gas fraction in the model is equal to the universal ratio, and simulate the gas evolution within DM haloes of a virial mass of $M_{vir} = 2 \times 10^8\, h^{-1}\,M_\odot$ and a virial radius $R_{vir} = 945\, h^{-1}$ pc. The initial temperature of the gas is taken to be $T = 3.2 \times 10^4$ K. The simulation domain is a box with a size $L_{box} = 6$ kpc centred on the halo. In the following, we abbreviate the spherical radii with R and cylindrical ones with r.

The initial DM and gas density profiles $\rho_{DM}(R)$ and $\rho_g(R)$ are those of an non-singular isothermal spheres with a flat density core of $R_{c,DM} = 0.34$ pc for DM and $R_{c,g} = 142.65$ pc for the gas, respectively (Fig. 1):

$$\rho_g(R) = \rho_{g,0} \begin{cases} \dfrac{1}{\left(1+\frac{R}{R_{c,g}}\right)^2} & (R \le R_{vir}) \\ \dfrac{1}{\left(1+\frac{R_{vir}}{R_{c,g}}\right)^2}\dfrac{R_{vir}^3}{R^3} & (R > R_{vir}), \end{cases} \quad (1)$$

$$\rho_{DM}(R) = \rho_{DM,0}\frac{R_{c,DM}^2}{R^2} \quad (R \le R_{vir}), \quad (2)$$

where $\rho_{DM,0} = 7.38 \times 10^{-18}$ g cm^{-3}, and $\rho_{g,0} = 1.66 \times 10^{-23}$ g cm^{-3}. Such DM haloes are similar to the NFW haloes (Navarro, Frenk & White 1997), and are simple to construct. The DM halo core size is actually set by the gravitational softening length for GADGET-3 SPH.

Table 1. Simulation parameters for the isolated halo models with ENZO AMR and GADGET-3 SPH. Name of the run and the values of spin parameter λ is listed. 'I' in the model abbreviation stands for isolated runs, and the number λ × 100 for DM haloes. Cosmological models (not shown in the table), are abbreviated by 'C' and by λ × 100.

Name: isolated	λ
AMR-I1	0.01
AMR-I3	0.03
AMR-I5	0.05
AMR-I7	0.07
SPH-I1	0.01
SPH-I3	0.03
SPH-I5	0.05
SPH-I7	0.07

The DM halo rotation is defined in terms of the cosmological spin parameter λ,

$$\lambda = \frac{J}{\sqrt{2} M_{\rm vir} R_{\rm vir} v_{\rm c}}, \tag{3}$$

where J is the total angular momentum of the DM halo, $M_{\rm vir}$ the halo virial mass, and $v_{\rm c}$ the circular velocity at $R_{\rm vir}$, which is constant with radius for an isothermal sphere mass distribution. The mean DM spin is $\lambda \sim 0.035 \pm 0.005$ (e.g. Bullock et al. 2001). We explore the range of $\lambda \simeq 0$–0.07 in our isolated models. For identical λ, we sample the same initial density distribution using four different random number sequences. The properties of the collapsing baryons have been averaged over these sequences. Models having identical mass distribution and differing only in the initial random sequence, are abbreviated similarly.

To produce the DM haloes with a pre-specified λ for isolated halo models, we follow the prescription of Long, Shlosman & Heller (2014). In short, we set the isotropic distribution of velocity dispersion in DM. Then we reverse tangential velocities for a fraction of DM particles to reproduce the specific angular momentum described above, with λ equal to the required value. For both SPH particles and the gas in AMR grid cells, we calculate the average tangential velocities of the background DM in cylindrical shells, accounting for the dependence along the (rotation) z-axis. The rotational velocities for the gas in the equatorial plane of the DM halo are given by

$$v_{\rm t}(r) = v_0 \times \begin{cases} r/R_{\rm c,g} & \text{if} \quad r \le R_{\rm c,g}, \\ 1 & \text{if} \quad R_{\rm c,g} \le r \le R_{\rm vir}, \end{cases} \tag{4}$$

where v_0 is tangential velocity defined by λ. The radial velocity dispersion in the centre is given by $\sigma = \sqrt{GM_{\rm vir}/2R_{\rm vir}} = 21.3\,{\rm km\,s^{-1}}$, where G is the gravitational constant. The isolated halo models have been listed in Table 1 and are identified with 'I' and the value of the spin parameter multiplied by 100. In cosmological models, we use the same notation, but replace 'I' with 'C'.

In the isolated models of GADGET-3, the DM resolution is set by the fixed gravitational softening length, $\epsilon_{\rm DM} = 0.37$ pc. This is done in order to match the condition in ENZO runs. For ENZO, it corresponds to an initial root grid of 64^3 in a 6 kpc region with a maximal refinement level of 8 allowed for gravity, $\epsilon_{\rm DM,min} = 6000/64/2^8 = 0.37$ pc.

For the gas, the gravitational softening is $\epsilon_{\rm g} = 10^{-4}$ pc, which is a fixed number for GADGET-3 and serves as a minimal value for ENZO. In other words, we use the initial resolution of 512^3 SPH particles or cells for baryons, and 100^3 particles or particles-in-mesh for the DM. All other parameters in ENZO and GADGET-3 runs are similar. The force resolution in adaptive PM codes is twice the minimal cell size (e.g. Kravtsov, Klypin & Khokhlov 1997). Isolated and cosmological runs and their parameters are summarized in Tables 1 and 2. We use the models AMR-I5 and SPH-I5 as representative isolated models.

Table 2. Summary of simulation setup for ENZO-2.4 (AMR) and GADGET-3 (SPH) simulations.

Parameters	Isolated model	Cosmological model
Simulation volume	6 kpc box	$3\,h^{-1}$ Mpc with a zoom-in region of $0.4\,h^{-1}$ Mpc
Initial baryonic resolution	64^3 root-grid with three levels of refinement; effective 512^3 zoom grid and SPH particles	256^3 root-grid and SPH particles; effective 2048^3 zoom grid and SPH particles
Number of DM particles	100^3	256^3 for outer region; effective 2048^3 for zoom region[a]
Mass resolution	$532.5\,{\rm M}_\odot$ for DM particles $0.7\,{\rm M}_\odot$ for gas particles	$245.7\,h^{-1}\,{\rm M}_\odot$ for DM particles $44.7\,h^{-1}\,{\rm M}_\odot$ for gas particles
Gravitational softening	$\epsilon_{\rm DM,min} = 0.37$ pc for DM in ENZO[b] $\epsilon_{\rm DM} = 0.37$ pc for DM in GADGET $\epsilon_{\rm g,min}$ = smallest cell size for gas in ENZO $\epsilon_{\rm g} = 10^{-4}$ pc for gas in GADGET	$\epsilon_{\rm DM,min} = 0.36\,h^{-1}$ pc for DM in ENZO[c] $\epsilon_{\rm DM} = 0.36\,h^{-1}$ pc for DM in GADGET $\epsilon_{\rm g,min}$ = smallest cell size for gas in ENZO $\epsilon_{\rm g} = 10^{-3}\,h^{-1}$ pc for gas in GADGET
Minimum gas smoothing length $\eta_{\rm min}$	10^{-3} pc	$10^{-2}\,h^{-1}$ pc[d]

[a]The size of the zoom-in region is about one-tenth of the outer region, therefore the actual grid/particle number in the zoom region is initially $\sim 200^3$ for both baryons and DM particles.
[b]Maximum refinement level for DM gravity is set to eight levels for ENZO in isolated models, i.e. $\epsilon_{\rm DM,min} = 6000/64/2^8 = 0.37$ pc. The isolated models do not have Hubble expansion in space, so there is no factor of h^{-1} and all numbers are physical.
[c]Maximum refinement level for DM gravity is set to 15 levels for ENZO in cosmological models, i.e. $\epsilon_{\rm DM,min} = 3 \times 10^6/256/2^{15} = 0.36\,h^{-1}$ pc.
[d]Maximum refinement levels for the gas in ENZO are set to 17 levels in isolated models and 20 levels in cosmological models.

2.3 Set-up in cosmological models

For further comparison, we use zoom-in cosmological simulations with the same composition as in isolated models to follow up the gas evolution within DM haloes. The ICs are generated using *WMAP*5 cosmology: $\Omega_\Lambda = 0.721$, $\Omega_\mathrm{m} = 0.279$, $\Omega_\mathrm{b} = 0.0445$, $h = 0.701$, $\sigma_8 = 0.807$, and $n = 0.961$. The models run from $z = 200$. The same cooling packages have been used for cosmological models as for isolated ones (Section 2.1).

For the initial set-up, we use the MUSIC algorithm (Hahn & Abel 2011) to generate cosmological zoom-in ICs. MUSIC uses a real-space convolution approach in conjunction with an adaptive multigrid Poisson solver to generate highly accurate nested density, particle displacement, and velocity fields suitable for multiscale zoom-in simulations of structure formation in the universe.

Generating a set of zoom-in ICs is a two-step process. First, we generate $3\,h^{-1}$ Mpc comoving 256^3 DM-only ICs for the pathfinder simulation and run it without AMR until $z = 10$. Using the HOP group finder (Eisenstein & Hut 1998), we select an appropriate DM halo, whose mass is $\gtrsim 10^8\,h^{-1}\,\mathrm{M}_\odot$ at $z = 10$. Secondly, we generate $0.4\,h^{-1}$ Mpc ICs with 2048^3 effective resolution in DM and gas, embedded in the lower resolution outer region. Since we use the same random seeds for these ICs as the first step, the phases of both ICs are identical. The zoom-in region is centred on the selected halo position and is set to be large enough to cover the initial positions of all selected halo particles. We perform the zoom-in procedure for each of the targeted haloes.

In the cosmological runs, the gravitational softening is 10^{-3} pc in the comoving coordinates, in the SPH run. We have measured the spin parameter of many haloes in the range of $\lambda \sim 0.01$–0.07 in our zoom region at $z \sim 10$, and use $\lambda \sim 0.04$ as a representative one for both AMR and SPH runs.

3 RESULTS

We aim at comparing results for direct baryonic collapse within DM haloes by ENZO-2.4 AMR and GADGET-3 SPH codes. As a first step, we compare the isolated models. The cosmological haloes have a range of spin parameter, as discussed in Section 2.2. To match the conditions of these haloes, we generate isolated haloes with the same range of λ (Table 1 and Section 3.1). The cosmological haloes are examined in Section 3.2. Lastly, we test the effect of λ on the dynamics of the collapse in isolated and cosmological models (Sections 3.3 and 3.4).

3.1 Direct collapse in isolated models

Direct collapse of isolated models with atomic gas has been performed and analysed by Choi et al. (2013) for $\lambda = 0.05$, using ENZO. Many of the aspects of its evolution are generic. We define $t = 0$ at the start of the run, and stop the run when the central collapse reaches the final resolution of $R_\mathrm{fin} \sim 10^{-3}$ pc, in both ENZO and GADGET-3, in order to allow a meaningful comparison, because the SPH run would have difficulty reaching a higher resolution without invoking complicated procedures, such as SPH particle splitting.

The DM in isolated models has isothermal profiles by construction, i.e. $\rho_\mathrm{DM} \propto R^{-2}$. They remain nearly identical to ICs. As the collapse proceeds and reaches the central region, the DM is dragged inwards by the gas, and is compressed adiabatically, forming new cusps with slopes ~ -1 to ~ -2.

The baryonic collapse proceeds in two stages, which are representative for all isolated models. First, the gas cools down to the cooling floor of atomic gas, then collapses following a self-similar solution, analogous to the Larson–Penston solution for an isothermal self-gravitating gas cloud, $\rho \propto R^{-2}$ (Larson 1969; Penston 1969). But significant differences are obvious, as angular momentum is present and modifies the solution, and the DM dominates the gravitational potential everywhere during the initial stage.

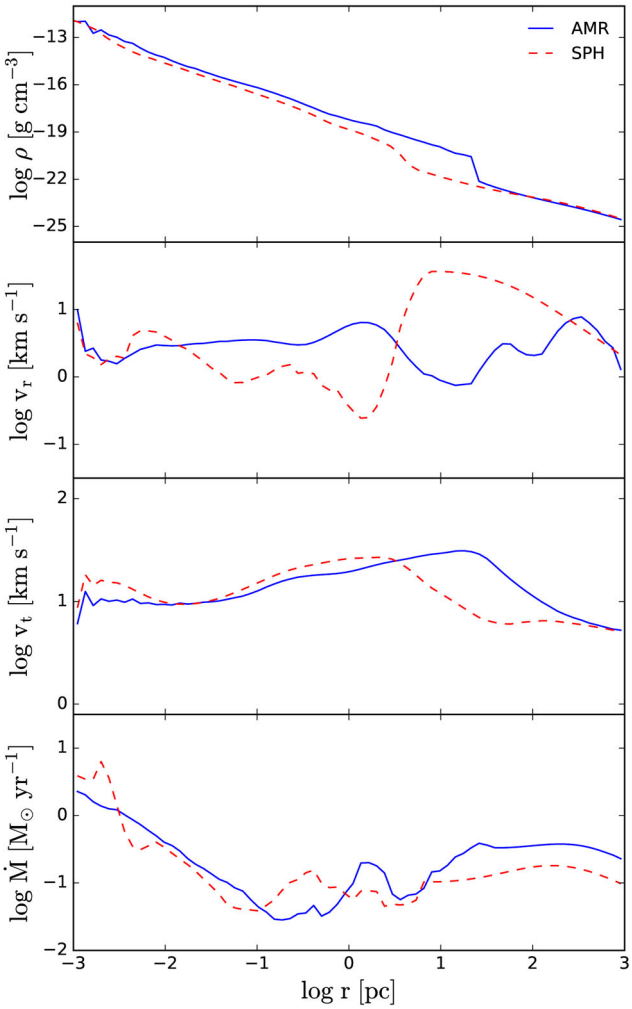

Figure 2. From top to bottom, radial profiles of gas density, radial velocity, tangential velocity, and mass accretion rate, at the end of the isolated runs for models AMR-I5 (solid lines) and SPH-I5 (dashed lines). All axes are logarithmic. The density and accretion rates have been averaged over spherical shells, and the velocities averaged over cylindrical shells.

When collapsing gas reaches the centrifugal barrier, a shock forms, where the density jumps and the radial velocity drops abruptly (top panels of Fig. 2). The gas accumulates behind the shock and forms a disc which grows in mass. As the gas density in the inner disc surpasses that of the DM, the second stage of the collapse ensues, and proceeds with an increasingly short time-scale. Basically, most of the gas behind the shock collapses and reaches the prescribed resolution of $\sim 10^{-4}$ pc (e.g. Choi et al. 2013), although here we compare the final distributions when $R_\mathrm{fin} \sim 10^{-3}$ pc has been reached.

The current AMR simulations with various λ follow basically the same outline. The initial positions of shocks in all runs are located at ~ 1 pc, and move out with time. The radial positions of these shocks

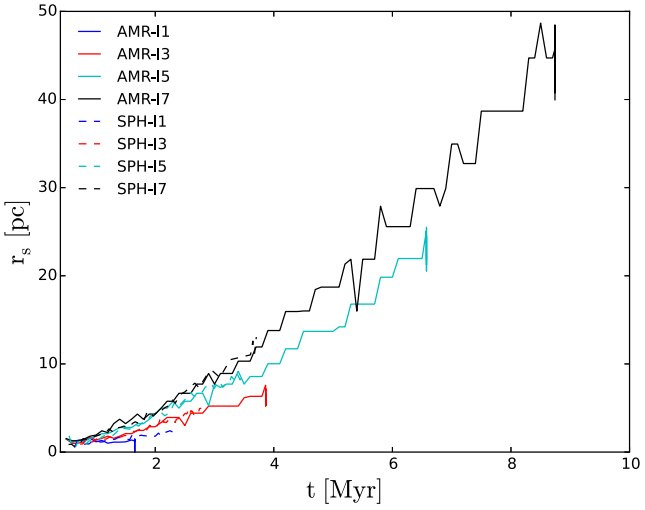

Figure 3. Evolution of the radial position of shocks, r_s, in isolated models in ENZO (solid lines) and GADGET-3 (dashed lines) runs for various λ. Note that both AMR and SPH runs with the same λ exhibit the same $r_s(t)$. The maximal r_s correspond to the end of the simulation.

also increase with increasing spin parameter, λ, as the centrifugal barrier is reached at progressively larger radii. Fig. 3 displays the shock locations as function of time, from their formation time to the end of the simulations. Note, that for a specific λ, both AMR and SPH shocks strictly follow each other. Moreover, consistently, the AMR shocks reach larger radii, as shown in Fig. 3 for all λ. The explanation for this difference comes from the fact that the isolated AMR models collapse later than the isolated SPH models, as we discuss below, and shocks have more time to advance.

As a first step, we compare the radial profiles of a gas density, radial and tangential velocities, and accretion rates at the end of the runs, i.e. when the collapse has reached $R_{\rm fin}$ (Fig. 2). All values are given after averaging in cylindrical or spherical shells and at the run end. The gas density and accretion rates have been averaged over spherical shells, and the velocities averaged over cylindrical shells. Shown are the representative AMR-I5 and SPH-I5 runs. In AMR-I5 run, the gas goes through a strong accretion shock and forms a disc, ending the first stage of the collapse. By the end of the runs, the SPH-I5 shock is positioned at a radius about three times smaller than in the AMR-I5, which is confirmed by Fig. 3. It appears also somewhat weaker than the AMR shock. In all other respects, the gas density profiles are very similar, albeit it takes another decade in radius for the density in SPH-I5 to catch up with the AMR-I5 density just inside the shock. The final density is $\rho \sim 10^{-14}\,{\rm g\,cm^{-3}}$ at $R_{\rm fin} = 10^{-3}$ pc.

The radial velocity profiles, v_r, are very similar in the outer few hundred pc. In the pre-shock region, both v_r increase towards the centre, then fall down substantially to a deep minimum in the post-shock region, at the respective positions of the shocks in the AMR and SPH runs. At smaller radii of $r < 10^{-2}$ pc, the curves are very similar and increase by an order of magnitude towards $R_{\rm fin}$. The tangential velocities, v_t, reach maximal values in the post-shock region of both runs, as expected, then decrease towards the centre. The behaviour of v_r and v_t with r is associated with a variable degree of rotational support with radius, as we discuss below.

The mass accretion rate profiles show a similar behaviour, but $\dot{M}$ differs by a factor of 3 in the pre-shock region, where $\dot{M} \sim 0.6\,{\rm M_\odot\,yr^{-1}}$ for the AMR run and $\sim 0.2\,{\rm M_\odot\,yr^{-1}}$ for the SPH run. This rate drops to below $\sim 0.1\,{\rm M_\odot\,yr^{-1}}$ at $R < 10$ pc for both runs. The second stage of the collapse inside $\sim$0.1 pc displays a nearly identical behaviour – both curves show a linear growth with decreasing r, reaching $\dot{M} \sim 0.5\,{\rm M_\odot\,yr^{-1}}$ at $R_{\rm fin}$. The small spike in the SPH run at $r \sim 10^{-3}$ pc is caused by insufficient mass resolution there.

The projected gas volume density shown in Fig. 4 emphasizes both similarities and differences, in comparison with the 1D radial density profiles. The most significant difference is that of the central disc size in the top frames – disc radius of $\sim$20 pc in the AMR-I5, and only $\sim$7 pc in the SPH-I5. This difference clearly has its origin in the position of the radial shock in both runs, as discussed above. So both discs appear shock-bounded. In the top frames, we also see a pronounced spiral structure in the AMR run, and a weaker one in the SPH run. The same conclusion can be reached from 5-pc scale images (middle and bottom panels), where $m = 2$ (gaseous bar) is seen within the central 0.3 pc, and $m = 3$ mode is driving a triple spiral on scales $\gtrsim$0.5 pc. The SPH-I5 run displays comparable $m = 2$ and 3 modes on the same scales.

Redistribution of the angular momentum is an important ingredient of gravitational collapse. We compare specific angular momenta, j_z, in the gas at the end of the simulations, in AMR-I5 and SPH-I5 (Fig. 5). Two important differences can be observed. Positions of radial shocks (Fig. 2) corresponds to the radii where the specific angular momenta curves come close to the circular angular momenta, $j_z \sim j_c$. At smaller radii, j_z moves away from j_c gradually. Still, there is a non-negligible rotational support at $R_{\rm fin}$, in both runs, albeit smaller for the SPH-I5 run. The bottom frames of this figure provide the quantitative measure of rotational support in the form of j_z/j_c radial profiles. The AMR exhibits a disc at larger radii than the SPH run, because it takes more time for the AMR model to collapse, and, therefore, the accretion shock has more time to propagate outwards. In the second stage of the collapse, i.e. inside $\sim$1 pc, the j_z/j_c ratio declines inwards, and showing a plateau for $\lesssim 10^{-2}$ pc, at about 0.5. They demonstrate that, in the isolated models, rotational support for the collapsing gas never falls below $\sim$50 per cent in the second stage, in both runs.

The T–ρ_g relation is shown in Fig. 6 at the end of the representative AMR-I5 and SPH-I5 runs. While the upper envelope of T is similar in both models, there appears to be much more gas at lower T at low densities, $\rho < 10^{-20}$ g cm^{-3}, in the AMR-I5 run. Given our refinement criteria, this is an anticipated property of mesh codes which are able to follow the low-density gas, while SPH codes tend to resolve better the higher density regions. On the other hand, a larger amount of low-T gas appears to be present at high densities, $\sim 10^{-18}$–10^{-17} g cm^{-3}, in the SPH-I5 run. We note that AMR run has larger mass accumulated (at $\rho \sim 10^{-20}\,{\rm g\,cm^{-3}}$) around the shock, due to a larger shock radius, as evident from Fig. 3. Since we use identical cooling packages for all runs, this difference can arise from the ability of numerical schemes to resolve the shocks and the cooling of a post-shock gas. In the AMR-I5, the radial shock is strong and advances to larger radii corresponding to lower gas densities of $\sim 10^{-21}\,{\rm g\,cm^{-3}}$. The low-$T$ gas is formed from the post-shock gas which cools down more efficiently. On the other hand, the SPH-I5 shock is weaker and happens at $\sim 10^{-19}\,{\rm g\,cm^{-3}}$, where particles at lower T already are much more common. Hence the shocked particles' contribution is hardly visible on the phase diagram.

Fig. 7 compares various parameters which affect the resolution in AMR and SPH runs. The left-hand panel shows evolution of maximal density in the gas, $\rho_{\rm max}$, with time. Clearly, the collapse in

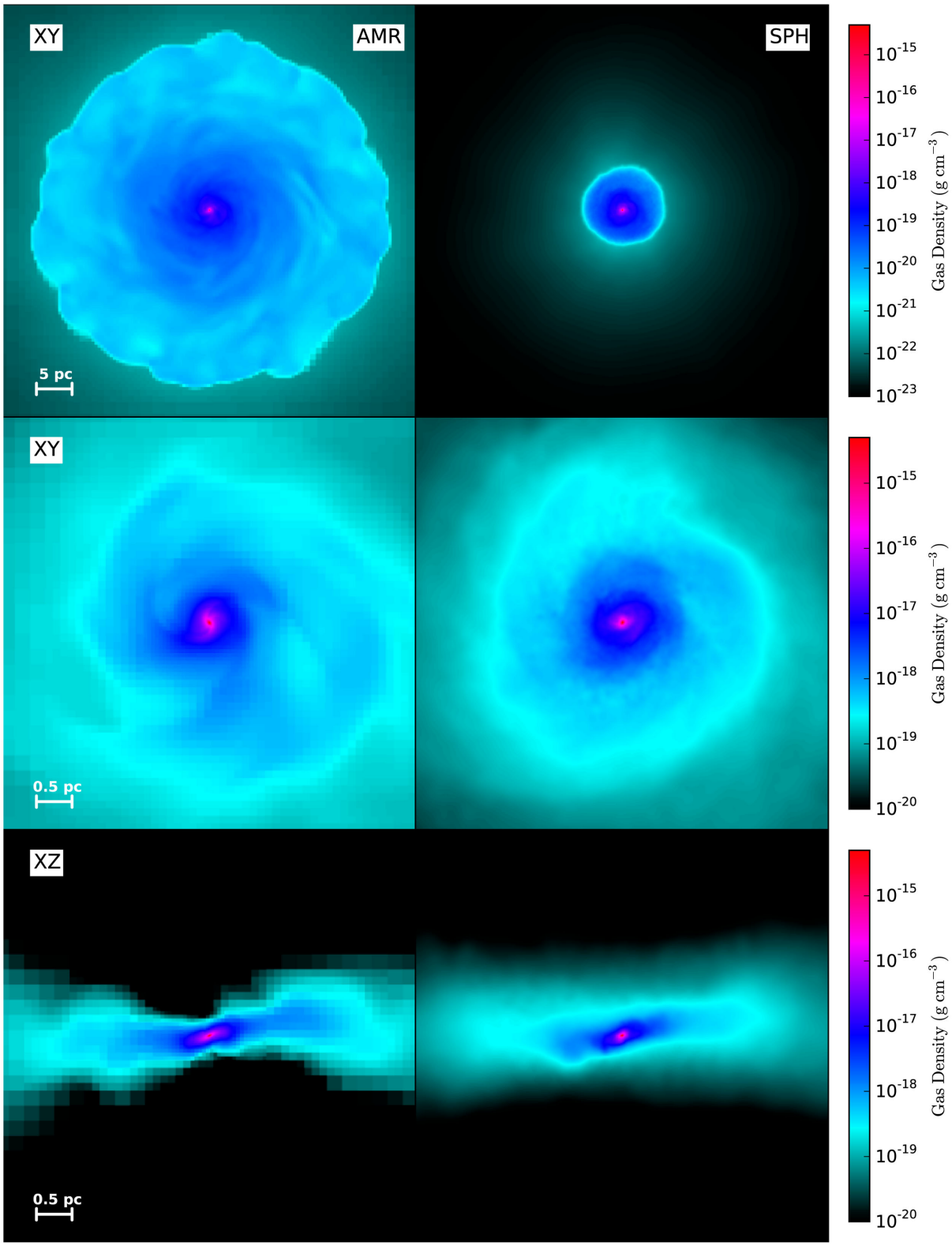

Figure 4. Mass-weighted gas volume density in the *x*–*y* equatorial plane (top and middle frames) and the *x*–*z* plane (bottom) of isolated models AMR-I5 (left frames) and SPH-I5 (right frames), at the end of the runs. Shown are the snapshots of decreasing spatial scales (physical): 50 pc (top) and 5 pc (middle and bottom) on each side, respectively. The colour palette reflects the range from minimum to maximum densities in each panel. The face-on and edge-on discs can be seen clearly in both runs.

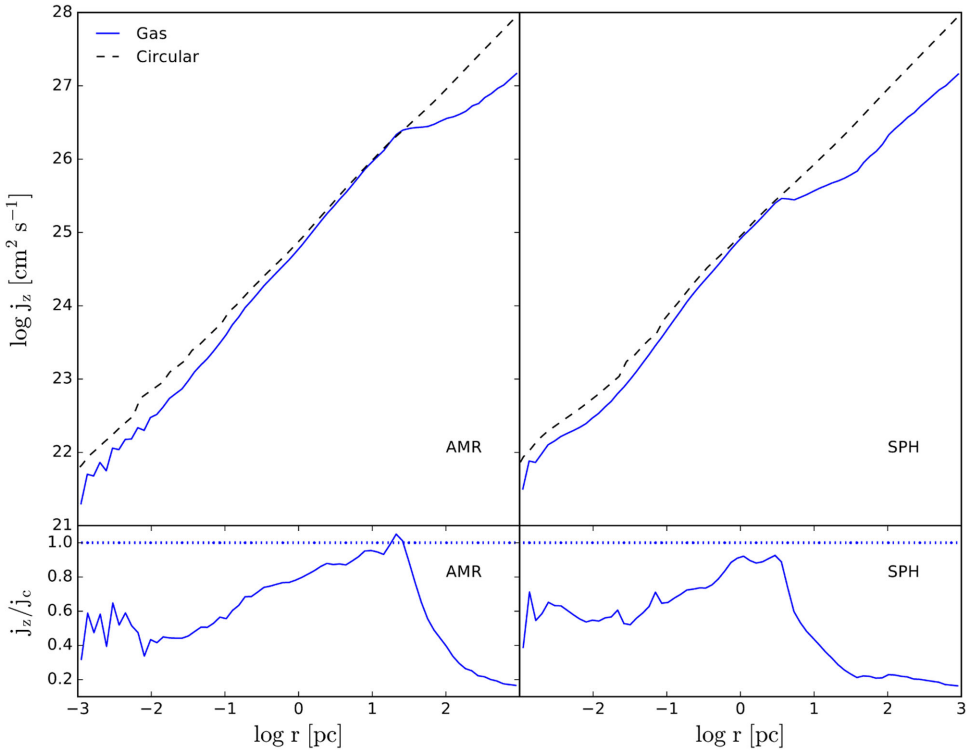

Figure 5. Specific angular momentum profile in the gas as a function of cylindrical radius for AMR-I5 (left-hand panel) and SPH-I5 (right-hand panel). Circular angular momentum profile is shown for comparison (dashed line).

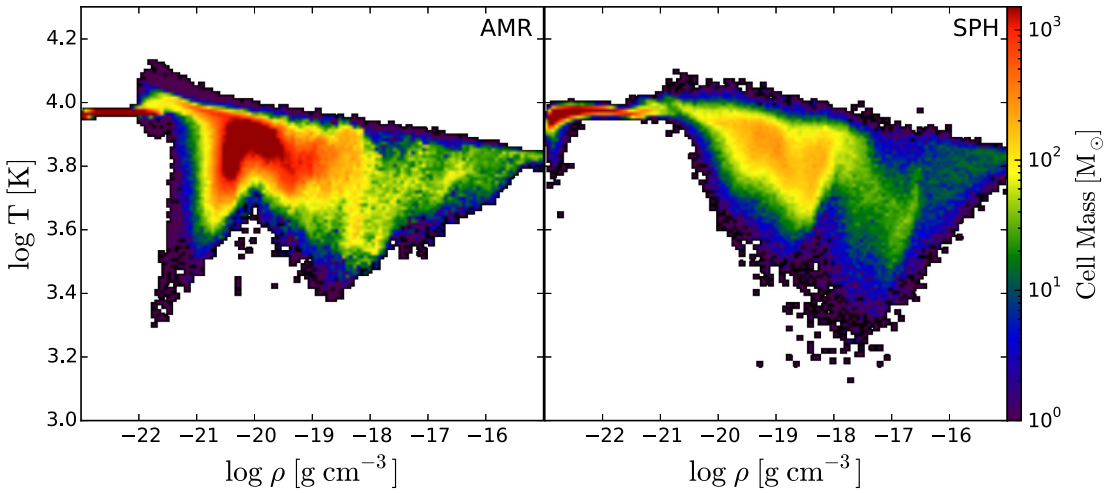

Figure 6. Phase diagram of temperature versus density of gas in isolated runs AMR-I5 (left-hand panel) and SPH-I5 (right-hand panel) at the end of each run. The colour represents the amount of mass in each pixel.

the isolated model SPH-I5 proceeds much faster than in AMR-I5 already during the first stage. At the onset of second stage, the density increases slowly, exhibiting kind of a plateau, then accelerates, and at the end of this stage $\rho_{\rm max}$ increases rapidly. Both runs display an identical behaviour at the end.

The evolution of $\rho_{\rm max}$ allows us to quantify the separation of the two stages of the collapse (see also Choi et al. 2013). The plateau between the stages provides an independent quantitative support to the existence of these stages. They are also observed in the evolution of the minimum gas smoothing length for SPH and minimum cell size for AMR, $\eta_{\rm min}$, shown in the middle frame of Fig. 7 – this frame describes the same process of $\rho_{\rm max}$ but in terms of the gas minimal smoothing length $\eta_{\rm min}$, which is the minimal interparticle distance. Following Choi et al. (2013, 2015) and Shlosman et al. (2016), we choose to define the beginning of the second stage when the gas-to-DM density ratio becomes larger than unity within the central few pc. This happens at $t \sim 2.4$ Myr in SPH-I5 and ∼6.3 Myr in AMR-I5. The collapsing gas reaches the final resolution of $\eta_{\rm min} \sim$ few $\times\ 10^{-3}$ pc at ∼2.4 Myr and ∼6.3 Myr, respectively. At this time the collapse has reached $r_{\rm fin}$.

The final radial profile of $\eta_{\rm min}$ is shown in the right-hand panel of Fig. 7. Both AMR and SPH curves for $\eta_{\rm min}$ are similar, but still the AMR one is systematically lower by a factor of 2–3 depending on the radius.

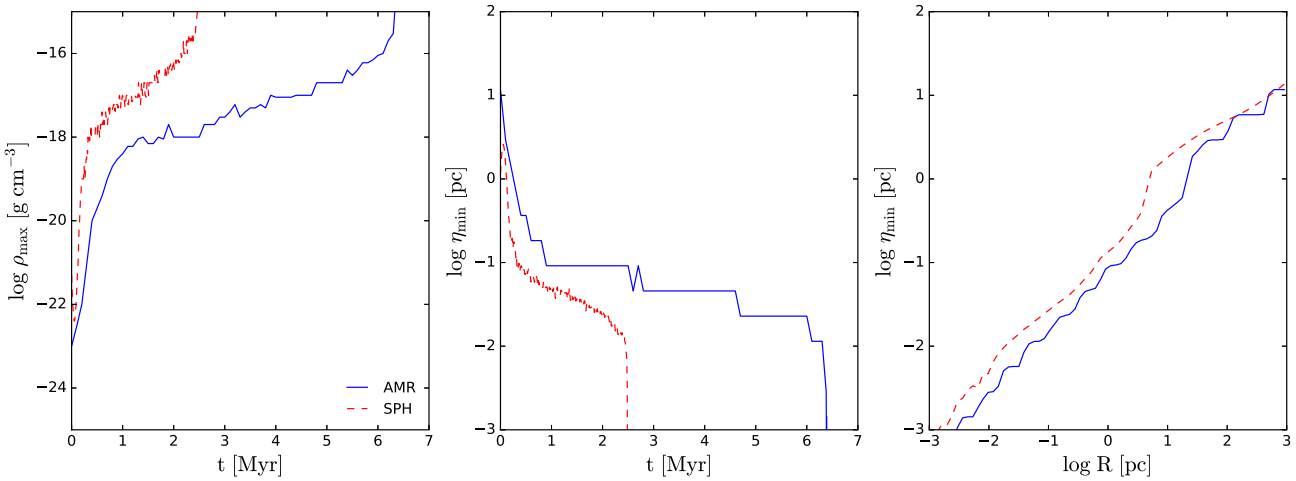

Figure 7. Comparing various resolution parameters for isolated models AMR-I5 (solid lines) and SPH-I5 (dashed lines). Left-hand panel: evolution of maximum gas density ρ_{max} as a function of time. Middle panel: evolution of the minimal gas smoothing length for the SPH and minimum cell size for the AMR run, η_{min}, as functions of time. Right-hand panel: radial profile of resolution given by the smoothing length for SPH and the minimum cell size at *each* radius for AMR, at the end of the runs. The first stage of the collapse which starts at $t = 0$ is identical for both models. The second stage of the collapse is triggered when the gas-to-DM density ratio in the inner few pc exceeds unity, i.e. ∼2.4 Myr for GADGET and ∼6.3 Myr for ENZO. Note, that after the onset of the second stage of the collapse, the collapse proceeds on a very short time-scale as observed by the sharp drop in η_{min} (middle panel).

3.2 Direct collapse in cosmological models

For cosmological models, we stop the runs when the AMR and SPH resolutions, measured by η_{min}, reach $R_{fin} \sim 10^{-2}$ pc. The reason for this is that high resolution of isolated models is more difficult to reach in cosmological runs. Therefore, we reduce the resolution demands in both AMR and SPH cosmological models by a factor of 10 compared to the isolated ones. The time is measured from the big bang.

As the DM haloes form and grow with time in the cosmological models, the DM density profiles tend to the NFW shape (Navarro et al. 1997). When the collapse reaches the central regions, the baryon drag in the DM and form a cusp, similar to that in isolated models. Note, that our isolated models follow the isothermal sphere density profiles and not the NFW ones. We shall return to this issue in Section 4.

We show the gas density, radial and tangential velocity, and mass accretion rate profiles for representative cosmological models AMR-C4.2 and SPH-C4.2 with $\lambda \sim 0.042$ – very similar to the representative isolated cases (Fig. 8). We have also measured the DM halo virial masses and virial radii for ENZO and GADGET cosmological models at the time of direct collapse, z_{coll} (Table 3). Overall, the AMR models collapse slightly earlier than the SPH ones. Consequently, the DM haloes appear slightly less massive and their virial radii slightly smaller. So a pronounced trend exists between the AMR and SPH cosmological models.

The top panel displays the final density profiles which are remarkably similar for the two runs. While density at $R_{fin} \sim 10^{-2}$ pc is nearly identical to that in the corresponding isolated runs, the overall shape of $\rho(R)$ somewhat differs. In the isolated runs, inside the radial shock, the slope of $\rho(R)$ was nearly constant, while in the cosmological runs it exhibits the trend of becoming shallower with R. This change happens at $R \sim 0.5$–5 pc, continues inwards, and appears slightly more pronounced in AMR than in the SPH runs. It appears to be the result of our use of an isothermal density profile for the DM in isolated models, and the formation of less cuspy NFW DM profiles in the cosmological runs. Another major difference between isolated and cosmological models is the absence of standing radial shock, which we explain below.

The radial velocities in AMR-C4.2 and SPH-C4.2 vary within a factor of a few along r, but end up similar within a factor of 2 at the centre. The tangential velocity is consistently higher in AMR at $r \gtrsim 0.2$ pc, then reverse the trend with the AMR velocity becomes smaller than SPH one at $r \lesssim 0.2$ pc.

The bottom panel of Fig. 8 displays the radial profile of mass accretion rate, $\dot{M}$. The curves differ by a factor ∼2–3 among themselves, in the outer radii, and $\lesssim$2 inside 50 pc. But they also differ profoundly from their isolated counterparts. First they exhibit a deep minimum at $r \sim$ 50–100 pc and stay about constant, $\dot{M} \sim$ 1–3 $M_\odot$ yr^{-1} inwards. The reason for this behaviour is increased rotational support they experience in this region, i.e. v_r and v_t have local minima and maxima there. On the other hand, the isolated models display growing $\dot{M}$ towards r_{fin} and reach a maximum there which is greater than the cosmological case by a factor of 2. The cosmological $\dot{M}$ is higher by a factor of a few everywhere except at the very centre. Lastly, at the centre, for $R \lesssim 0.1$ pc, the mass accretion in the SPH run falls by almost an order of magnitude, and less so in the AMR run.

Fig. 9 compares the projection snapshots for DM and volume densities for the gas of representative cosmological simulations from identical ICs for ENZO (left-hand panels) and GADGET-3 (right-hand panels). The extracted DM haloes have $\lambda = 0.042$. The snapshots have been taken at the end of the runs, when the collapse have reached $R_{fin} \sim 0.01$ pc. The top panels show the large-scale distribution of the DM on scales of $100\,h^{-1}$ kpc (comoving). Some differences are noticeable in these frames, and typically can be attributed to individual DM haloes. Indeed, we focus on the representative DM haloes in the second row within (approximately) their virial radii, with the box size of $5\,h^{-1}$ kpc (comoving). Again, while overall a nice degree of similarity exists between the two runs, differences are clear as well, especially if one focuses on the substructure on this scale. The bottom panels show the corresponding gas distribution within these haloes, on scales of $200\,h^{-1}$ pc (comoving). While the AMR panel displays the characteristic filamentary structure, the SPH panel shows a rather centrally-concentrated elongated

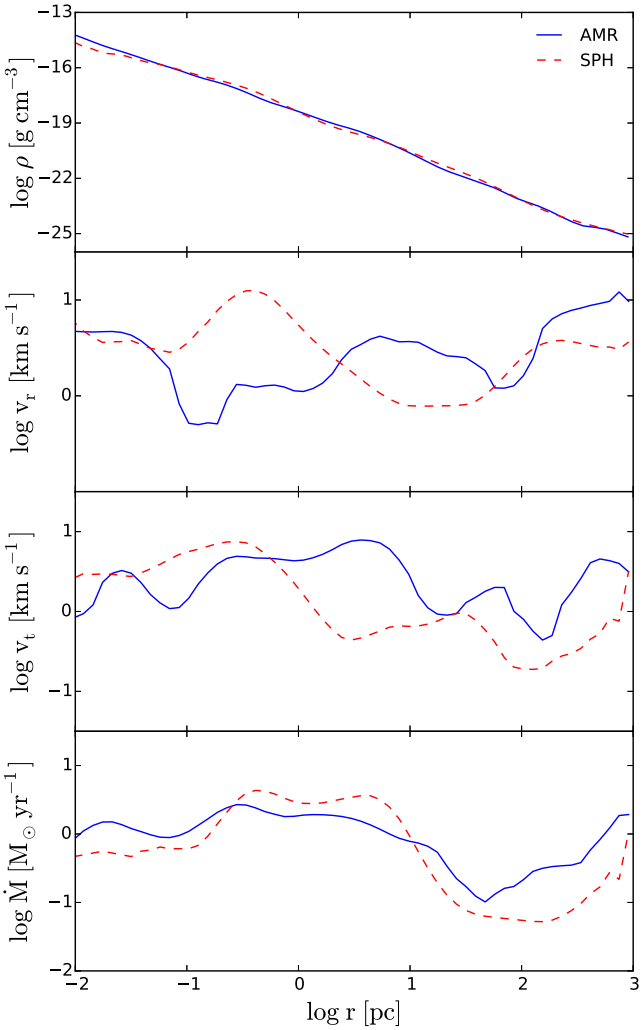

Figure 8. From top to bottom, radial profiles of gas density, radial velocity, tangential velocity, and mass accretion rate, at the end of the cosmological runs for models AMR-C4.2 (solid lines) and SPH-C4.2 (dashed lines). All axes are logarithmic. The density and accretion rate have been averaged over spherical shells, and velocities averaged over cylindrical shells.

Table 3. DM halo virial parameters in AMR and SPH cosmological models at the time of direct collapse, i.e. at $z_{\rm coll}$.

Models	$z_{\rm coll}$	$M_{\rm vir}$ (h^{-1}M$_\odot$)	$R_{\rm vir}$ (h^{-1}pc)
AMR-C1.5	17.2	2.4×10^7	407
AMR-C2.8	11.9	4.7×10^7	722
AMR-C4.2	19.3	2.7×10^7	379
SPH-C1.5	15.5	4.1×10^7	538
SPH-C2.8	11.0	5.4×10^7	809
SPH-C4.2	18.6	3.4×10^7	422

gas distribution, although the central density is the same in both runs. The SPH density distribution displays less small-scale structure in general. The AGORA collaboration (Kim et al. 2014) has also reported difference in substructure within the similar large-scale structure.

Next, we show the radial distribution of the specific angular momentum profile at the end of the simulations, as well as j_z/j_c ratio (Fig. 10). Clearly, both runs display much less angular momentum support at all radii compared to the isolated models. On top of this, the SPH run shows even less support than the AMR one, and proceeds basically in the free-fall fashion until it has reached $r \sim 0.1$ pc. The explanation for such a dramatic difference between the rotational support in isolated and cosmological models is related to the efficiency of angular momentum extraction from the gas by the background DM. In the former models, the DM haloes are nearly axisymmetric, while in the latter case, they are substantially triaxial. Resulting gravitational torques from the DM on to the gas will be largely suppressed in the isolated models, and the gas will have stronger rotational support.

We also show the comparison between the T–ρ maps for the above models in Fig. 11. The overall feature of the phase diagrams are very similar between the two runs, with the exception of the mass involved at particular T and ρ values. At high densities, the AMR run shows a somewhat broader distribution in T-range with very small mass contained in each grid-cell, which are completely absent in the SPH run. This is understandable, as the two codes have a different resolution at these densities. Although we start from identical ICs in ENZO and GADGET-3, the refinement history differs between the codes in detail. We have tested how sensitive is the evolution with respect to the refinement condition in ENZO and discuss it below.

To specify the characteristic times of gravitational collapse in the cosmological models, we follow the definition from isolated models. The onset of the first stage of the collapse is inferred from the sudden rise in refinement level in ENZO and from $\eta_{\rm min}(t)$ in GADGET. The second stage is triggered when the gas-to-DM density ratio exceeds unity in both ENZO and GADGET.

The left-hand panel of Fig. 12 shows the time evolution of $\rho_{\rm max}$ in cosmological simulations. The time prior to $t \sim 178$ Myr corresponds to DM structure formation. It involves the initial expansion and collapse of DM shells, forming a small DM halo, which we target in the zoom-in simulations. This halo grows via accretion of cold gas and DM – a process permeated by merger events. As the halo approaches the critical mass of $\sim 10^8$ M$_\odot$, direct baryonic collapse follows. The gas collapse starts around 178 Myr and proceeds rapidly (but slower than in the isolated models), being triggered nearly simultaneously in both runs.

The middle frame of Fig. 12 displays the evolution of the minimal smoothing length, $\eta_{\rm min}$, in the gas. Again, until the onset of the gravitational collapse, the AMR curve displays a better resolution compared to the SPH one, by a factor of 2–3, but both codes are resolving basically the same densities at this time (see Section 4 for more details). This difference appears during the initial collapse and formation of the targeted DM halo. With the onset of direct collapse at $t \sim 178$ Myr, this difference in $\eta_{\rm min}$ gets amplified and the collapse proceeds increasingly faster in the AMR run. This is a reverse situation with respect to isolated models, and shows up explicitly in the radial profiles of $\eta_{\rm min}$. We expect that the run with a smaller $\eta_{\rm min}$ will collapse first. We note that the duration of the baryonic collapse here, $\sim$10–20 Myr, is substantially longer than in respective isolated models. The reason for this difference comes from the collapse inside NFW haloes which have a substantially lower central DM densities than in similar isothermal spheres used by us for isolated models.

The right frame of Fig. 12 displays the radial profile of $\eta_{\rm min}(R)$ at the end of cosmological simulations AMR-C4.2 and SPH-C4.2. Note, the bifurcation in $\eta_{\rm min}$ at around few pc from the centre of the DM halo. Whereas the outer halo region is equally resolved with both runs, the inner one is better resolved with the AMR. This explains why the second stage of the collapse proceeds faster with ENZO.

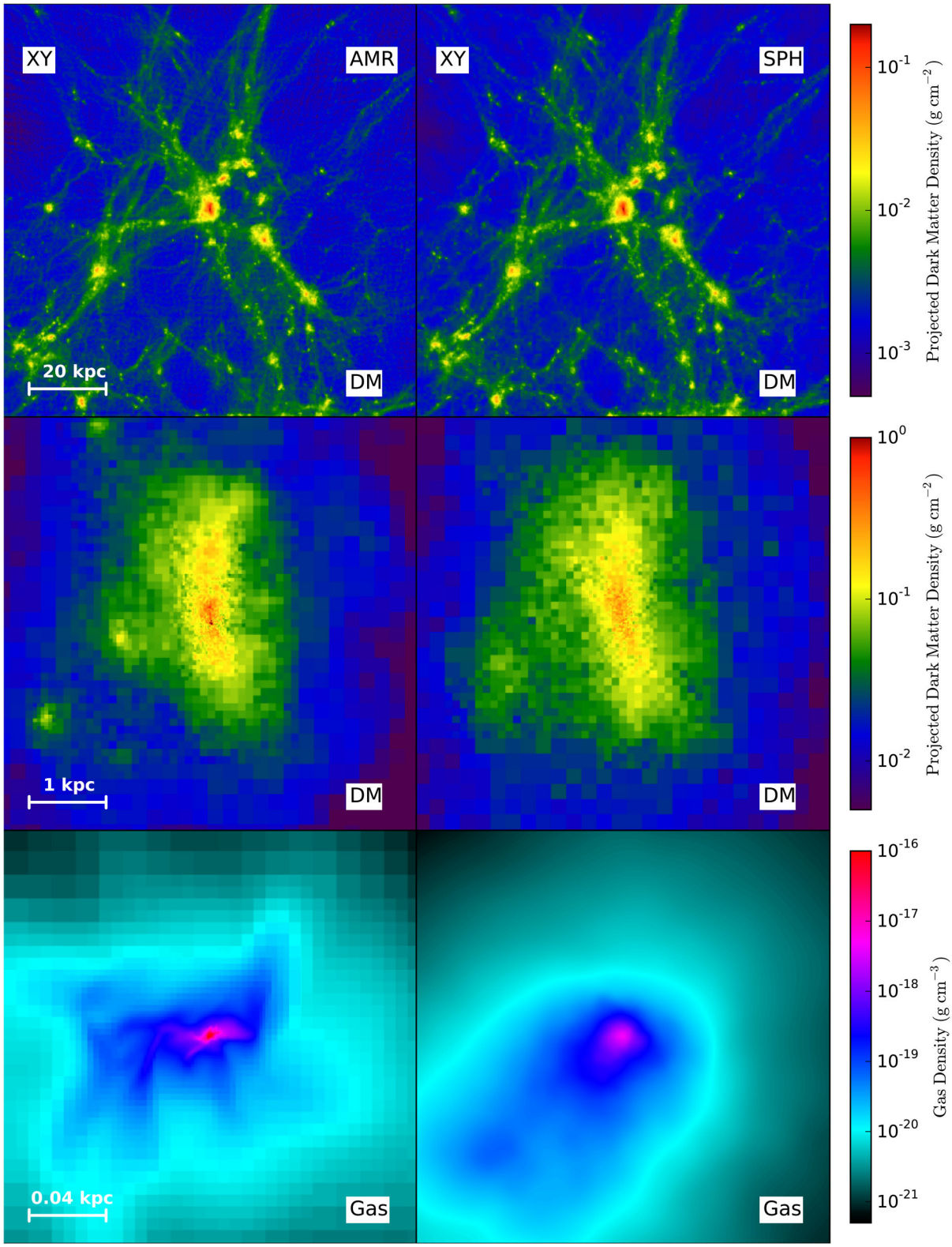

Figure 9. Projections of final DM density in x–y plane in cosmological models AMR-C4.2 (left-hand column) and SPH-C4.2 (right-hand column). The spatial scale of each panel decreases from top to bottom: DM in 100 kpc (comoving), DM in 5 kpc (comoving), and mass-weighted gas volume density in 200 pc (comoving), respectively. The depth of each frame is 10 kpc (top), and 0.5 kpc (middle) in comoving coordinates. The colour palette reflects from minimum to maximum projection densities in each panel.

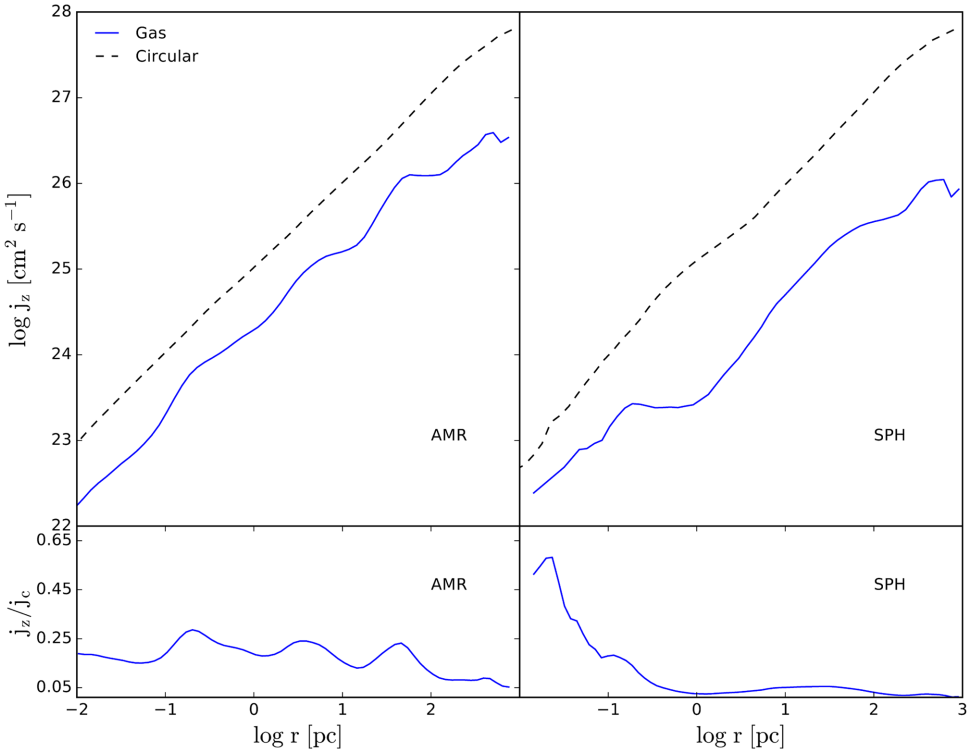

Figure 10. Specific angular momentum profile of gas as function of cylindrical radius for ENZO (left-hand panel) and GADGET3 (right-hand panel) in the cosmological runs AMR-C4.2 and SPH-C4.2. Circular angular momentum profile is shown for comparison (dashed line).

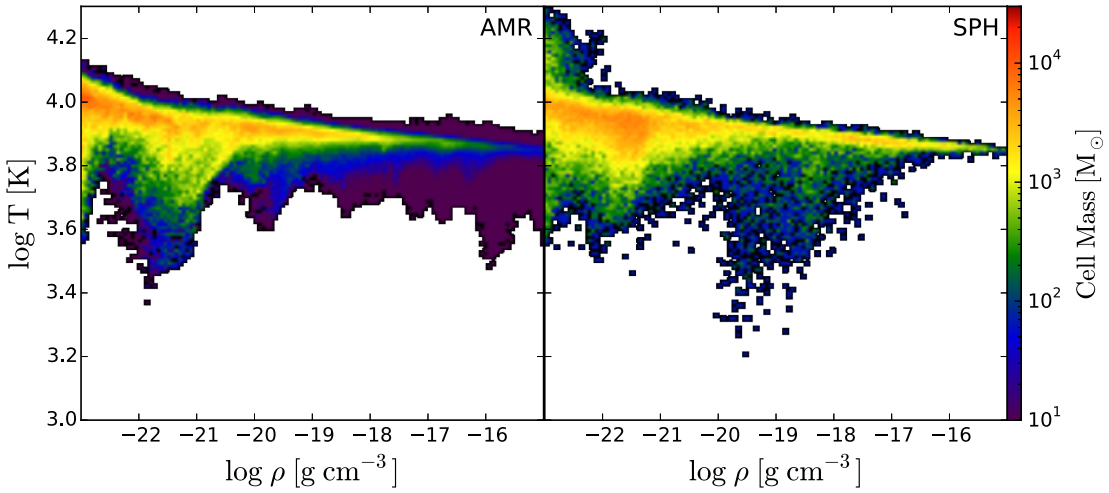

Figure 11. Phase diagram of temperature versus density in AMR-C4.2 (left-hand panel) and SPH-C4.2 (right-hand panel) at the end of the cosmological model simulations. The colour represents the mass in each pixels.

3.3 Effect of host DM halo spin on isolated models

As additional and a broad test for model comparison, we measure the collapse time in each model and contrast the ENZO-2.4 and GADGET-3 runs in isolated models. Effect of gas rotation on gravitational collapse has been also modelled by Jappsen et al. (2009) in the context of Pop III star formation. However, they assumed a *rigid* spherical DM halo which, therefore, cannot absorb angular momentum and/or produce gravitational torques on the gas.

To analyse the collapse time for isolated models, we measure the time from the start of the run, using models with a range in the spin parameter λ, for AMR and SPH runs. In other words, we define the collapse time, Δt_c, as the time from $t = 0$ till the collapse reaches $R_{\rm fin} = 10^{-3}$ pc (Section 2.2). The collapse time, Δt_c, is given in Fig. 13.

For isolated models, two trends can be observed. First, both AMR and SPH runs exhibit a monotonic increase of Δt_c with λ, up to the measured spin of $\lambda \sim 0.07$ (Fig. 13). Secondly, the AMR runs display a longer collapse time than the SPH runs. As a corollary, the difference between the collapse time of AMR and SPH runs is increasing monotonically with λ.

The first trend can be easily explained. With increasing DM halo spin parameter, the gas must overcome a centrifugal barrier positioned at progressively larger radii, because the ICs for the isolated

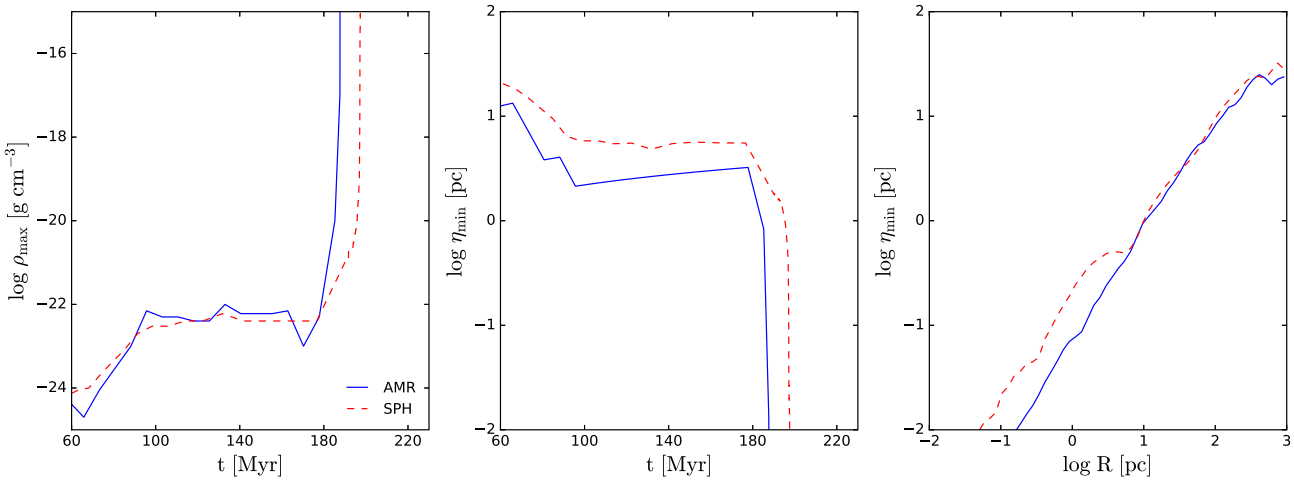

Figure 12. Same as Fig. 7, but for cosmological models AMR-C4.2 (solid lines) and SPH-C4.2 (dashed lines). Note, that the collapse starts around $t \sim 178$ Myr for AMR and SPH runs, when ρ_{max} and η_{min} are slightly in favour of the AMR, compared to being identical in the isolated models. $\eta_{min}(R)$ shows that the innermost resolution is higher in ENZO inside few central pc, while it is identical in the outer DM halo.

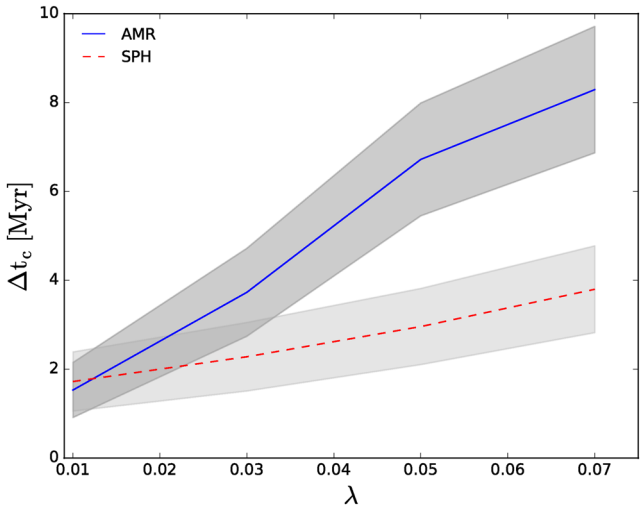

Figure 13. Duration of gravitational collapse time for isolated models, Δt_c, in ENZO-2.4 and GADGET-3 runs as function of the halo spin parameter λ. The grey region represents $\pm 1\sigma$ errors using the Poisson statistics.

runs require the gas to have the same specific angular momentum $j(r)$ distribution as the DM. The gas evolution is complicated by the intricacies of gravitational collapse: gas at small radii collapses first and it has lower j than the gas at larger radii. So the initial circularization determines the position of the accretion shock which forms at $\sim$1 pc from the centre, as seen in Fig. 3. As the gas with larger j circularizes at larger r progressively later, the shock moves out, and does it faster for larger λ. Hence, the size of the forming disc behind the accretion shock is increasing with λ and with time (e.g. Fig. 3).

For the second stage of the collapse to ensue, the gas must decouple from the background DM potential, i.e. its density must increase above the DM density at small radii (e.g. section 3.1 of Choi et al. 2015). In isolated models this is approximately the radius of the disc which forms behind the standing accretion shock. Naturally, a larger accumulation of baryons is required when decoupling happens at larger radii, explaining the increased Δt_c for larger λ. Indeed, the disc sizes and, therefore, masses increase with λ.

Hence, this simple physics explains the relatively modest increase in Δt_c with λ. Remarkably, both ENZO and GADGET-3 runs agree in their Δt_c for $\lambda = 0.01$. But what about the increasing delay in the collapse time of the AMR runs with λ? To understand this, one should look carefully into different resolution pattern of both codes. While ICs are identical in this respect, the SPH gravitational softening is constant with time, while that of the AMR code are refined as the collapse proceeds. This by itself does not have a direct effect on the dynamics, but there are caveats. Probably the most important issue is the possible effect that refinement has on the development on degree of turbulence in the collapsing gas.

In Fig. 14(a), we show evolution of η_{min} for three representative λ for ENZO and GADGET-3. For $\lambda = 0.01$, $\eta_{min}(t)$ displays little difference between ENZO-2.4 and GADGET-3. For higher spin, we observe an increasing delay in the second stage of the collapse, especially for ENZO runs. Checking the associated increase in the refinement levels, the latter appears to stagnate before the onset of the second stage of the collapse. In other words, η_{min}, which reflects the best spatial resolution at each time, as mentioned above, 'hesitates' to decrease for a longer time in ENZO compared to GADGET-3. Therefore, we observe a longer plateau for ENZO in Fig. 14.

3.4 Effect of host DM halo spin on cosmological models

In the previous section, we have measured the collapse time-scales for isolated models and contrasted them between ENZO-2.4 and GADGET-3 runs. Similar exercise in cosmological models is more complicated, because it involves cosmological evolution of DM haloes, which depends on structure formation in the universe and results in haloes having different shapes and other properties. Hence, while a detailed comparison of the collapse time for cosmological models is outside the scope of this work, we do compare some numerical aspects of their evolution with various λ.

We define the cosmological collapse time-scale, Δt_c by following the evolution of the baryonic refinement level, the maximal hydrodynamic resolution, η_{min}, and the maximal density, ρ_{max} – all defined as in isolated models. The beginning of the direct collapse in the cosmological DM haloes, t_0, is determined when these parameters exhibit a sharp increase or decrease, correspondingly. For example, η_{min} decreases sharply at $t \sim 178$ Myr, which is considered as the onset of the collapse. The end point of the collapse is

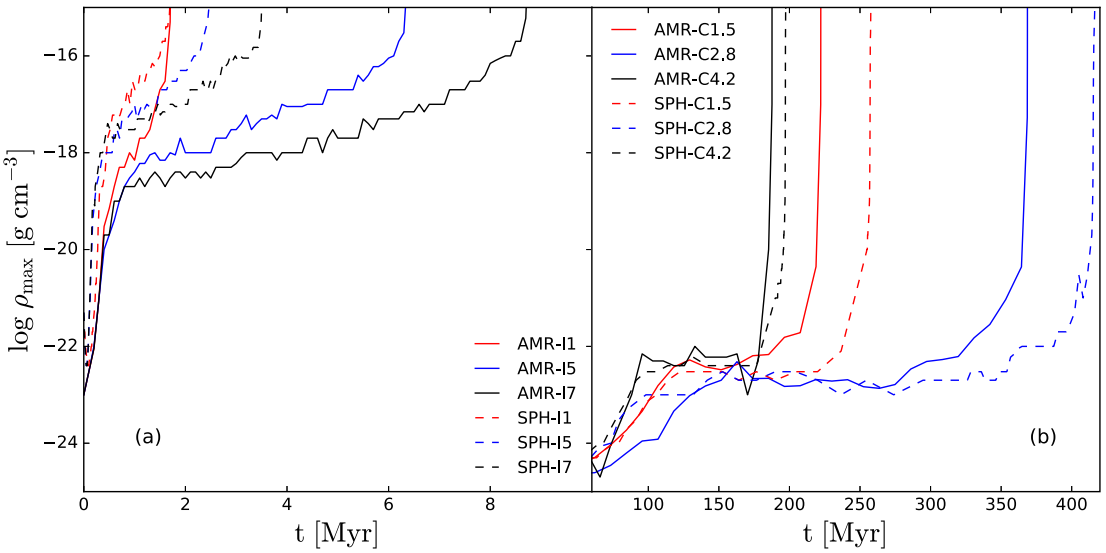

Figure 14. Comparison of the evolution of $\rho_{\rm max}(t)$ for (a) three isolated models with $\lambda = 0.01$, 0.05, and 0.07 for AMR-I1, -I5, and -I7 (solid lines) and SPH-I1, -I5, and -I7 (dashed lines) runs; (b) same for three cosmological models, AMR-C1.5, - C2.7, and -C4.2 (solid lines) and SPH-C1.5, -C2.7, and -C4.2 (dashed lines). The collapse time-scales, $\Delta t_{\rm c}$, for these models are listed in Table 4.

Table 4. Values of $\Delta t_{\rm c}$ for isolated and cosmological models shown in Fig. 14. The definitions of $\Delta t_{\rm c}$ are given in Sections 3.3 and 3.4 for isolated and cosmological models, respectively.

Models	$\Delta t_{\rm c}$ (Myr)
AMR-I1	1.7
AMR-I5	6.3
AMR-I7	8.3
SPH-I1	1.7
SPH-I5	2.3
SPH-I7	3.4
AMR-C1.5	14.6
AMR-C2.8	17.5
AMR-C4.2	14.3
SPH-C1.5	20.6
SPH-C2.8	19.8
SPH-C4.2	20.6

taken $t_{\rm fin}$, when it reaches $R_{\rm fin}$, and $\Delta t_{\rm c} = t_{\rm fin} - t_0$. To detect a sharp increase/decrease in $\rho_{\rm max}$ and $\eta_{\rm min}$, we follow their time derivatives after ∼140 Myr and test all the occurrences for the increase/decrease by a factor of 2 or more.

We repeat the λ-test discussed in the previous section, for cosmological models. Naively, one expects to observe the same correlation between $\Delta t_{\rm c}$ and λ shown in Table 4 and in Fig. 13. However, as exhibited by Fig. 14(b), this is not the case. For three representative cosmological models in AMR and SPH, the one-to-one correlation between $\Delta t_{\rm c}$ and λ does not exist here. Why does this happen?

A number of physical reasons in cosmological models would 'mess up' this correlation. First, the host DM haloes in isolated models are axisymmetric. This means that collapsing gas has difficulty to lose angular momentum to DM, and loses it mostly to gas. On the other hand, the DM halo shapes in cosmological models differ profoundly from axisymmetric shapes. Therefore, the gas will lose its angular momentum continuously and efficiently to the DM, which will move the gas away from the centrifugal barrier at each radius, as in fact is shown in Fig. 10.

Secondly, because the direct collapse takes about 10–20 Myr in cosmological models, the basic properties of DM haloes can change during this time. They can undergo minor, intermediate, and major mergers. In other words, the host haloes will have enough time to interact with the substructure – which does not happen in isolated models.

These and additional factors are expected to affect the direct collapse onset and duration in cosmological simulations in a kind of unpredictable way, which we indeed observe in our simulations.

For isolated and cosmological SPH and AMR models, the free-fall time for the DM haloes at the onset of direct collapse is $t_{\rm ff} \sim$ 35 Myr. In comparison with the actual collapse time-scales given in Table 4, the collapse times are shorter than the free-fall times. This underlines an important point that direct collapse involves only the inner part of the gas initially residing in DM haloes.

4 DISCUSSION AND CONCLUSIONS

We have performed comparison simulations of gas collapse in DM haloes in the context of direct collapse scenario to form SMBH seeds using AMR and SPH codes. This problem involves large dynamic range, from kpc down to au scales – such a comparison has not been attempted before. Using ENZO-2.4 AMR and GADGET-3 SPH codes, we examined the systematic differences which build up when these numerical schemes are invoked. We made significant efforts to match the initial set-up of the two simulations. We addressed the associated problems using isolated and cosmological models of gravitational collapse in DM haloes with a range of cosmological spin parameter λ. To simplify this task, we ignored the effect of molecular hydrogen and UV background radiation, and assumed an optically-thin atomic cooling, as described in Sections 1 and 2. As a result, the collapse is nearly isothermal in all runs. Our main results are as follows.

(i) The isolated models generally follow similar evolutionary path and agree with Choi et al. (2013), but exhibit many subtle differences among themselves. Specifically, the collapse proceeds

in two stages, first reaching the angular momentum barrier, going through an accretion shock, and forming a disc behind it. In the second stage, which begins after the gas density in the disc region surpasses that of the DM density, the gas decouples from the background gravitational potential of the DM and experiences a runaway collapse, dragging some of the DM inwards in an adiabatic compression. We find that, although the AMR and SPH models start with identical ICs, the pace of increase in spatial resolution differs in both codes. This leads to a substantially earlier collapse in the SPH models for the isolated models.

(ii) Cosmological models do not exhibit 'standing' accretion shocks, unlike their isolated model counterparts, and, consequently, do not form rotationally-supported discs. The reason for this is the continuous loss of angular momentum by the collapsing gas to the background triaxial potential of the host DM haloes, contrary to isolated models which stay largely axisymmetric. Nevertheless, one can distinguish between first and second stages of the collapse, when the gas-to-DM density ratio crosses unity, within the central few pc. The cosmological evolution of DM haloes and baryons appears to be similar among the AMR and SPH runs, being only slightly in favour of the AMR models in baryonic spatial and mass resolutions. But a pronounced trend exists between the AMR and SPH cosmological models, with the former exhibiting direct collapse at higher redshifts, and, consequently, the collapse happens in less massive and smaller DM haloes. With the onset of baryonic gravitational collapse within DM haloes, the pace of the resolution change differs among the codes and the resolution increases faster in the AMR runs. Consequently, the trend in the time lag is reversed here with respect to the isolated models, and the AMR models collapse before the SPH models. Thus, a small difference in the pre-collapse resolution is amplified substantially during the collapse.

(iii) The collapse time Δt_c increases with increasing λ in isolated models. Greater centrifugal forces divert the infalling gas to larger radii, i.e. circularization happens further away from the rotation axis. This is translated to larger expansion velocities of the accretion shocks and larger accretion disc sizes. Shock in the AMR runs propagate further out than in the SPH runs, because the final collapse time is later for the AMR isolated models.

(iv) For cosmological models, the baryonic collapse time is much longer than in isolated models, because the average density in the central regions of the NFW haloes is lower than that of the isothermal spheres by a factor of $\sim$100, which leads to longer collapse time by a factor of $\sim$10. Additional factors discussed above affect Δt_c, unlike in isolated models.

In this work we have focused on numerical aspects of gravitational collapse to the SMBH seeds, and so avoid discussing the associated physics, except when unavoidable. The main reasons for dissimilar performance of the AMR and SPH codes lies in the mismatch between the pace of increase in spatial and mass resolutions when comparing performance of the AMR and SPH codes. These differences appear to be profound and not easily reconcilable.

Both numerical codes under comparison here, AMR ENZO-2.4 and SPH GADGET-3, follow collisionless cold DM and dissipative fluid component. Each of these components is important in order to understand evolution of gravitational collapse. The DM plays a crucial role in diluting the gravitational interactions within the gas, and, therefore, increasing its Jeans mass. Together with development of virial supersonic turbulence in the gas, it reduces the fragmentation in the collapsing flow, and allows the collapse to proceed via large dynamic range.

Most important is the resolution of the gravitational force. ENZO uses a multigrid PM method, and therefore, its resolution is governed by twice the minimum cell size (Section 2.2). On the other hand, GADGET-3 uses the tree method to compute gravity, and its gravitational resolution is set by a fixed softening length. Hence, the forces are computed more accurately in GADGET-3 compared to ENZO, particularly at the initial stage of collapse, when ENZO has not refined many levels yet. In principle, one should be able to make the ENZO gravity resolution comparable to that of GADGET from the very beginning, by investing significantly larger number of initial mesh allocations, e.g. by nested initial grid. However, this was not feasible with reasonable computational resources for this work.

In isolated models, we have been able to push the initial spatial resolution of ENZO to $\sim$10 pc with three initial nested grid levels. At the same time, GADGET has had a constant softening length of $\epsilon_g = 10^{-4}$ pc for the SPH particles and $\epsilon_{DM} = 0.37$ pc for the DM, from the beginning (see Table 2). Of course the particles are not as close as these distances from the start of the run, but the forces are computed accurately with the tree method down to ϵ_g and ϵ_{DM}. On the other hand, ENZO gravity was allowed to refine, but it did not refine fast enough to catch up with GADGET in the isolated models, judging from the evolution of the hydrodynamical resolution parameter, η_{min}. For periods of time, ENZO refinement level has been constant, then changed abruptly. Thus, ENZO resolution always lagged behind GADGET in the isolated models. Due to these differences, ENZO was unable to follow the steep density cusp of the DM isothermal sphere in the centre.

The above situation is similar to the one found in the context of cosmological simulation by O'Shea et al. (2005), where ENZO and GADGET codes have been compared for cosmological structure formation. In this case, ENZO had to invest in $\sim 256^3$ root-grid in order to reproduce the same DM halo mass function as the GADGET run with 128^3 particles. When simply using the root-grid of 128^3, ENZO was unable to follow the growth of early density perturbations due to poorer force resolution, and it resulted in an underestimate of halo substructures and low-mass haloes at early times. This means that ENZO AMR code requires significantly larger computing resources than GADGET SPH code in order to obtain similar structures on small scales, particularly in the context of cosmological structure formation.

In this work, the context and the spatial scale of the problem is very different from that of O'Shea et al. (2005). ENZO's main advantage is the refinement method which allows it to obtain a superior hydrodynamic or gravitational force resolution, albeit towards the end of the cosmological simulation and in a very small volume. Therefore, during the pre-collapse phase, when high resolution is not required, the difference in computational resources used by both codes are comparable, within a factor of 2, in the CPU time. On the other hand, during the direct collapse in isolated and cosmological models, GADGET requires 5–10 times more CPU time than ENZO. Compared to ENZO, GADGET overresolves in the initial stage of the collapse, and underresolves in the final stages, unless SPH particle splitting method is used or the SPH has a dynamic gravitational softening, as in GIZMO (e.g. Heller & Shlosman 1994; Hopkins 2013).

The bottom line is that in our simulations of direct baryonic collapse in isolated and cosmological framework, GADGET requires greater investment in computational resources, but benefits from better hydrodynamic and gravitational force resolution in the computational box, while ENZO achieves a superior resolution in a very small volume.

Note that our cosmological models of direct collapse evolve similarly in the AMR and SPH cases. The left-hand and middle panels of Fig. 12 show that direct collapse happens nearly simultaneously in AMR and SPH runs, as exhibited by the behaviour of $\rho_{\rm max}$ and $\eta_{\rm min}$. But these two parameters differ by a factor of a few until the onset of the direct collapse at $t \sim 178$ Myr. As the collapse develops, we observe that SPH lags behind AMR, unlike in isolated models, where the SPH models collapse first. The reason for this behaviour can be observed in the right-hand panel of Fig. 12. Here the AMR has higher mass and spatial resolution than SPH in the inner few pc at the final phase of the collapse.

The delay in the collapse time can have a significant impact on the cosmological evolution of direct collapse, in the presence of an external UV background. The latter can dissociate H_2 molecules, which is considered to be a critical factor for the success of this scenario (e.g. Omukai 2001; Latif, Zaroubi & Spaans 2011; Inayoshi, Omukai & Tasker 2014; Sugimura, Omukai & Inoue 2014). If the collapse is delayed significantly, it might appear favourably for the direct collapse scenario because of the higher UVB intensity from nearby star formation, which should be increasing with time at redshifts $z \sim 20$–10. In our current simulations, ENZO-2.4 and GADGET-3 give mixed results on the cosmological collapse time-scales, as we have discussed above. This happens because the cosmological collapse depends on realistic properties of DM haloes, such as their shapes. In a more controlled environment of isolated models, GADGET-3 exhibits earlier direct collapse than ENZO-2.4, due to the difference in the early force, mass, and hydrodynamic resolution between the two codes.

In summary, we have performed a comparison between the AMR code ENZO-2.4 and the SPH code GADGET-3 in the framework of direct collapse to SMBH seeds, using both isolated and fully cosmological models of the collapse. We have followed the model evolution into a strongly non-linear regime, when small initial differences have been substantially amplified. Although the overall model evolution has been found similar at large, substantial differences also exist at the end of the runs. We find that the main cause for these differences lies in different evolutionary pace of mass and spatial resolution with time and space. This results in different abilities of the numerical schemes to resolve hydrodynamics and gravitational interactions, such as shocks and angular momentum transfer by gravitational torques.

ACKNOWLEDGEMENTS

We thank the ENZO and YT support team for help. All analysis has been conducted using YT (Turk et al. 2011; http://yt-project.org/). We have used the GRACKLE chemistry and cooling library (Bryan et al. 2014; Kim et al. 2014, https://grackle.readthedocs.org/). We are grateful to Volker Springel for providing us with the original version of GADGET-3, and to Jun-Hwan Choi and Long Do Cao for their help in the early phase of this project. KN acknowledges the partial support by JSPS KAKENHI grant number 26247022. IS acknowledges partial support from STScI grant AR-12639.01-A. IS and KN are grateful to the support from the International Joint Research Promotion Program at Osaka University. Support for HST/STScI AR-12639.01-A was provided by NASA through a grant from the STScI, which is operated by the AURA, Inc., under NASA contract NAS5-26555. Numerical simulations were in part carried out on XC30 at the Center for Computational Astrophysics, National Astronomical Observatory of Japan, as well as the VCC at the Cybermedia Center at Osaka University.

REFERENCES

Abel T., Anninos P., Zhang Y., Norman M. L., 1997, New Astron., 2, 181
Abel T., Bryan G. L., Norman M. L., 2002, Science, 295, 93
Agertz O. et al., 2007, MNRAS, 380, 963
Anninos P., Zhang Y., Abel T., Norman M. L., 1997, New Astron., 2, 209
Ascasibar Y., Yepes G., Müller V., Gottlöber S., 2003, MNRAS, 346, 731
Balsara D. S., 1995, J. Comput. Phys., 121, 357
Barnes J., Hut P., 1986, Nature, 324, 446
Bate M. R., Burkert A., 1997, MNRAS, 288, 1060
Begelman M. C., Rees M. J., 1978, MNRAS, 185, 847
Begelman M. C., Shlosman I., 2009, ApJ, 702, L5
Begelman M. C., Volonteri M., Rees M. J., 2006, MNRAS, 370, 289
Begelman M. C., Rossi E. M., Armitage P. J., 2008, MNRAS, 387, 1649
Berger M. J., Colella P., 1989, J. Comput. Phys., 82, 64
Bromm V., 2013, Rep. Prog. Phys., 76, 112901
Bromm V., Larson R. B., 2004, ARA&A, 42, 79
Bromm V., Loeb A., 2003, ApJ, 596, 34
Bryan G. L., Norman M. L., 1997, in Clarke D. A., West M. J., eds, ASP Conf. Ser. Vol. 123, Computational Astrophysics: 12th Kingston Meeting on Theoretical Astrophysics. Astron. Soc. Pac., San Francisco, p. 363
Bryan G. L., Norman M. L., Stone J. M., Cen R., Ostriker J. P., 1995, Comput. Phys. Commun., 89, 149
Bryan G. L. et al., 2014, ApJS, 211, 19
Bullock J. S., Dekel A., Kolatt T. S., Kravtsov A. V., Klypin A. A., Porciani C., Primack J. R., 2001, ApJ, 555, 240
Choi J.-H., Shlosman I., Begelman M. C., 2013, ApJ, 774, 149
Choi J.-H., Shlosman I., Begelman M. C., 2015, MNRAS, 450, 4411
Colella P., Woodward P. R., 1984, J. Comput. Phys., 54, 174
Cullen L., Dehnen W., 2010, MNRAS, 408, 669
Eisenstein D. J., Hut P., 1998, ApJ, 498, 137
Ferland G. J. et al., 2013, Rev. Mex. Astron. Astrofis., 49, 137
Fraser M., Casey A. R., Gilmore G., Heger A., Chan C., 2015, preprint (arXiv:1511.03428)
Frenk C. S. et al., 1999, ApJ, 525, 554
Haehnelt M. G., Rees M. J., 1993, MNRAS, 263, 168
Hahn O., Abel T., 2011, MNRAS, 415, 2101
Heller C. H., Shlosman I., 1994, ApJ, 424, 84
Hirano S., Hosokawa T., Yoshida N., Umeda H., Omukai K., Chiaki G., Yorke H. W., 2014, ApJ, 781, 60
Hopkins P. F., 2013, MNRAS, 428, 2840
Hosokawa T., Omukai K., Yoshida N., Yorke H. W., 2011, Science, 334, 1250
Inayoshi K., Omukai K., Tasker E., 2014, MNRAS, 445, L109
Jappsen A.-K., Mac Low M.-M., Glover S. C. O., Klessen R. S., Kitsionas S., 2009, ApJ, 694, 1161
Johnson J. L., Khochfar S., Greif T. H., Durier F., 2011, MNRAS, 410, 919
Kim J.-H. et al., 2014, ApJS, 210, 14
Komatsu E. et al., 2009, ApJS, 180, 330
Koushiappas S. M., Bullock J. S., Dekel A., 2004, MNRAS, 354, 292
Kravtsov A. V., Klypin A. A., Khokhlov A. M., 1997, ApJS, 111, 73
Larson R. B., 1969, MNRAS, 145, 405
Latif M. A., Zaroubi S., Spaans M., 2011, MNRAS, 411, 1659
Latif M. A., Schleicher D. R. G., Schmidt W., Niemeyer J., 2013, MNRAS, 433, 1607
Loeb A., Rasio F. A., 1994, ApJ, 432, 52
Long S., Shlosman I., Heller C., 2014, ApJ, 783, L18
Madau P., Rees M. J., 2001, ApJ, 551, L27
Mayer L., Kazantzidis S., Escala A., Callegari S., 2010, Nature, 466, 1082
Milosavljević M., Bromm V., Couch S. M., Oh S. P., 2009, ApJ, 698, 766
Navarro J. F., Frenk C. S., White S. D. M., 1997, ApJ, 490, 493
Norman M. L., Bryan G. L., 1999, in Miyama S. M., Tomisaka K., Hanawa T., eds, Astrophys. Space Sci. Libr. Vol. 240, Numerical Astrophysics. Kluwer Academic, Boston, p. 19
O'Shea B. W., Nagamine K., Springel V., Hernquist L., Norman M. L., 2005, ApJS, 160, 1
Omukai K., 2001, ApJ, 546, 635

Penston M. V., 1969, MNRAS, 144, 425
Price D. J., Federrath C., 2010, MNRAS, 406, 1659
Prieto J., Jimenez R., Haiman Z., 2013, MNRAS, 436, 2301
Saitoh T. R., Makino J., 2013, ApJ, 768, 44
Schleicher D. R. G., Spaans M., Glover S. C. O., 2010, ApJ, 712, L69
Shapiro S. L., Teukolsky S. A., 1985, ApJ, 298, 58
Shlosman I., Choi J.-H., Begelman M. C., Nagamine K., 2016, MNRAS, 456, 500
Springel V., 2005, MNRAS, 364, 1105
Springel V., Hernquist L., 2003, MNRAS, 339, 289
Sugimura K., Omukai K., Inoue A. K., 2014, MNRAS, 445, 544
Tasker E. J., Brunino R., Mitchell N. L., Michielsen D., Hopton S., Pearce F. R., Bryan G. L., Theuns T., 2008, MNRAS, 390, 1267
Truelove J. K., Klein R. I., McKee C. F., Holliman J. H., II, Howell L. H., Greenough J. A., 1997, ApJ, 489, L179
Turk M. J., Abel T., O'Shea B., 2009, Science, 325, 601
Turk M. J., Smith B. D., Oishi J. S., Skory S., Skillman S. W., Abel T., Norman M. L., 2011, ApJS, 192, 9
Vogelsberger M., Sijacki D., Kereš D., Springel V., Hernquist L., 2012, MNRAS, 425, 3024
Volonteri M., Rees M. J., 2005, ApJ, 633, 624
Volonteri M., Rees M. J., 2006, ApJ, 650, 669
Wise J. H., Abel T., Turk M. J., Norman M. L., Smith B. D., 2012, MNRAS, 427, 311
Zel'dovich Y. B., Podurets M. A., 1965, Astron. Zh., 42, 963

This paper has been typeset from a TEX/LATEX file prepared by the author.